

ARTICLE

Open Access

Photoinduced large polaron transport and dynamics in organic–inorganic hybrid lead halide perovskite with terahertz probes

Zuanming Jin¹, Yan Peng¹✉, Yuqing Fang¹, Zhijiang Ye¹, Zhiyuan Fan¹, Zhilin Liu², Xichang Bao², Heng Gao³, Wei Ren³, Jing Wu⁴, Guohong Ma⁵, Qianli Chen⁶, Chao Zhang⁷, Alexey V. Balakin^{8,9}, Alexander P. Shkurinov^{8,9}, Yiming Zhu¹✉ and Songlin Zhuang¹

Abstract

Organic–inorganic hybrid metal halide perovskites (MHPs) have attracted tremendous attention for optoelectronic applications. The long photocarrier lifetime and moderate carrier mobility have been proposed as results of the large polaron formation in MHPs. However, it is challenging to measure the effective mass and carrier scattering parameters of the photogenerated large polarons in the ultrafast carrier recombination dynamics. Here, we show, in a one-step spectroscopic method, that the optical-pump and terahertz-electromagnetic probe (OPTP) technique allows us to access the nature of interplay of photoexcited unbound charge carriers and optical phonons in polycrystalline $\text{CH}_3\text{NH}_3\text{PbI}_3$ (MAPbI₃) of about 10 μm grain size. Firstly, we demonstrate a direct spectral evidence of the large polarons in polycrystalline MAPbI₃. Using the Drude–Smith–Lorentz model along with the Fröhlich-type electron-phonon (e-ph) coupling, we determine the effective mass and scattering parameters of photogenerated polaronic carriers. We discover that the resulting moderate polaronic carrier mobility is mainly influenced by the enhanced carrier scattering, rather than the polaron mass enhancement. While, the formation of large polarons in MAPbI₃ polycrystalline grains results in a long charge carrier lifetime at room temperature. Our results provide crucial information about the photo-physics of MAPbI₃ and are indispensable for optoelectronic device development with better performance.

Introduction

Organic–inorganic metal-halide perovskites (MHPs) are composed of organic cations and an inorganic framework. The success application of low-cost and solution-processable MHPs in optoelectronic devices can be attributed to low carrier recombination rates^{1,2}, ambipolar carrier transport^{3,4}, strong optical absorption^{5,6}, long

carrier diffusion^{7–9}, and inherent defect tolerance¹⁰. Given these advantages over conventional semiconductors, MHPs have attracted tremendous scientific research interest in recent ten years^{11,12}, for promising applications in cost-effective solar cells^{13–16}, solid-state lighting^{17–20}, transistors²¹, memristors²², and ultrafast spin switches in spintronics^{23,24}.

Despite that MHPs behave as defect-free semiconductors with low charge recombination rates, long diffusion lengths (1–3 μm), and long hot carrier lifetimes (1–3 μs) that exceed the Langevin limit for direct recombination, these materials show a moderate free charge-carrier mobility ($\mu \sim 30\text{--}100 \text{ cm}^2 \text{ V}^{-1} \text{ S}^{-1}$) comparing to other inorganic semiconductors. Efforts have been made to figure out such an apparent discrepancy in

Correspondence: Yan Peng (py@usst.edu.cn) or Yiming Zhu (ymzhu@usst.edu.cn)

¹Terahertz Technology Innovation Research Institute, Terahertz Spectrum and Imaging Technology Cooperative Innovation Center, Shanghai Key Lab of Modern Optical System, University of Shanghai for Science and Technology, Shanghai 200093, China

²Qingdao Institute of Bioenergy and Bioprocess Technology, Chinese Academy of Sciences, Qingdao 266101, China

Full list of author information is available at the end of the article

© The Author(s) 2022



Open Access This article is licensed under a Creative Commons Attribution 4.0 International License, which permits use, sharing, adaptation, distribution and reproduction in any medium or format, as long as you give appropriate credit to the original author(s) and the source, provide a link to the Creative Commons license, and indicate if changes were made. The images or other third party material in this article are included in the article's Creative Commons license, unless indicated otherwise in a credit line to the material. If material is not included in the article's Creative Commons license and your intended use is not permitted by statutory regulation or exceeds the permitted use, you will need to obtain permission directly from the copyright holder. To view a copy of this license, visit <http://creativecommons.org/licenses/by/4.0/>.

the dynamical carrier properties in MHPs^{25–27}. At room temperature, the interplay between carriers and ionic perovskite lattice is a possible microscopic mechanism behind this unusual recombination of photogenerated carriers in MAPbI₃²⁸. It was first proposed by Zhu and co-workers that large polarons—described as the charge carriers associated with the lattice deformation over several structural units—prevent scattering of photocarriers from charged defects, the remaining phonon bath, and other charge carriers in MHPs^{29–32}.

A number of spectroscopic and optical measurements, such as time-resolved optical Kerr effect spectroscopy, time-resolved two-photon photoemission, transient reflectance, and absorption spectroscopies, time-domain Raman spectroscopy, angle-resolved photoelectron spectroscopy, have been used to reveal the electron-phonon (e-ph) coupling in CsPbBr₃^{32–34}, MAPbBr₃^{35–37}, and MAPbI₃^{38–42}. However, these measurements are associated with the large polaron formation either from the phonon or from the electronic structure perspective^{42–44} (See Supplementary Table S1 for a literature survey). In addition, it is challenging, to use an ultrafast spectroscopic technique in the visible region to access the polaron mobility, carrier scattering parameters, and dynamics in MHPs quantitatively, which are considered as the fundamental nature of the large polaron^{29,45}.

In comparison with visible light, the frequencies of terahertz (THz) waves (ranging from several to tens of meV in energy scales) coincide with both the momentum relaxation times of conduction carriers^{46,47} and the typical optical phonons in MHPs^{48–50}. Thus, ultrafast THz spectroscopy is expected to be an appropriate approach to study the low energy excitations and the coupling between charge carriers and phonons. However, until now, researchers have relied on two THz spectroscopic approaches to characterize the large polaron behaviors in MHPs. On the one hand, the rise of the THz photoconductivity dynamics is observed after hot-carrier cooling, which has been ascribed to an indirect evidence of polaron formation⁵¹. On the other hand, the temperature dependence of scattering time $\sim T^{-3/2}$ supports a strong dependence of carrier transport on the phonons^{52–54}. This experimental behavior is inconsistent with the Fröhlich model, which predicts a temperature dependence $\sim T^{-0.46}$ of the polaron mobility⁵⁵. Therefore, the full potential of THz spectroscopic measurements for direct evidence of polaron formation in MAPbI₃ still remains to be shown.

We may also mention that quantitative characterization of the large polaron transport and dynamics in MHPs, requires the effective mass of the photoinduced charge carriers with renormalization factors due to polaron formation. A direct experimental method for determining the polaron mass in MHPs is the magneto-optical

spectroscopy by observing the Landau levels^{56,57}. For such measurements, a pulsed magnetic-field of 130 T⁵⁶ and a low temperature down to 1.5 K⁵⁷, are necessary. However, the small increase in the polaron mass cannot account for the moderate carrier mobility measured in MAPbI₃⁵⁷. Therefore, it is necessary to develop the capability to evaluate the backscattering probability of the carriers by traps and grain (or domain) boundaries on the ultrafast timescale^{58,59}. Nevertheless, a one-step characterization satisfying the requirements of room-temperature, magnets-free, access to the basic large polaron transport and ultrafast dynamics quantitatively is expected to be important, but has not been shown.

In this letter, we present a direct spectroscopic proof for the large polaron behavior due to the dynamic coupling between optical phonons and photocarriers in prototypical MAPbI₃ polycrystalline grains. To determine the large polaron mass and mobility, we take a completely different approach. We performed a contactless optical pump-THz electromagnetic probe (OPTP) measurement to obtain the complex-valued THz photoconductivity spectra $\tilde{\sigma}_s^{\text{pump}}(\omega)$ of MAPbI₃. The resonance-like spectral line shapes of the photoexcited THz conductivity response are inherently indicative of the coupling between the optical phonon modes and the photoinduced carriers, considered as large polarons. Following the Drude–Smith–Lorentz (DSL) model and the Fröhlich-type large polaron model, we are able to extract the effective mass and the carrier scattering parameters of the large polaron. Consequently, the large polaron mobility of MAPbI₃ is determined. It is found that the mass enhancement by polaron effect appears not to be significantly detrimental to the relatively low carrier mobility in MAPbI₃. Taking advantage of the OPTP time-resolved spectroscopy, we further demonstrate that the long-lived large polaronic carriers are the major photo-generated species in MAPbI₃ polycrystalline grains, which allows for efficient charge extraction. Our work provides important insights into the large polarons in MHPs, which is essential for developing energy and optoelectronic applications with better controlled charge-lattice interaction, charge-carrier mobilities, and transistor switching times.

Results

The samples used in this work are MAPbI₃ polycrystalline grains and thin films. Firstly, high-quality MAPbI₃ single-crystals were synthesized according to the literature^{60–62}. The photographs of the MAPbI₃ single crystal and the corresponding X-ray diffraction (XRD) pattern are given in Figs. S1 and S2, respectively. The prominent peaks at 14.6° and 28° correspond to (110) and (220) planes of MAPbI₃ single crystal. As very little THz signal could transmit through the thick single crystal, the

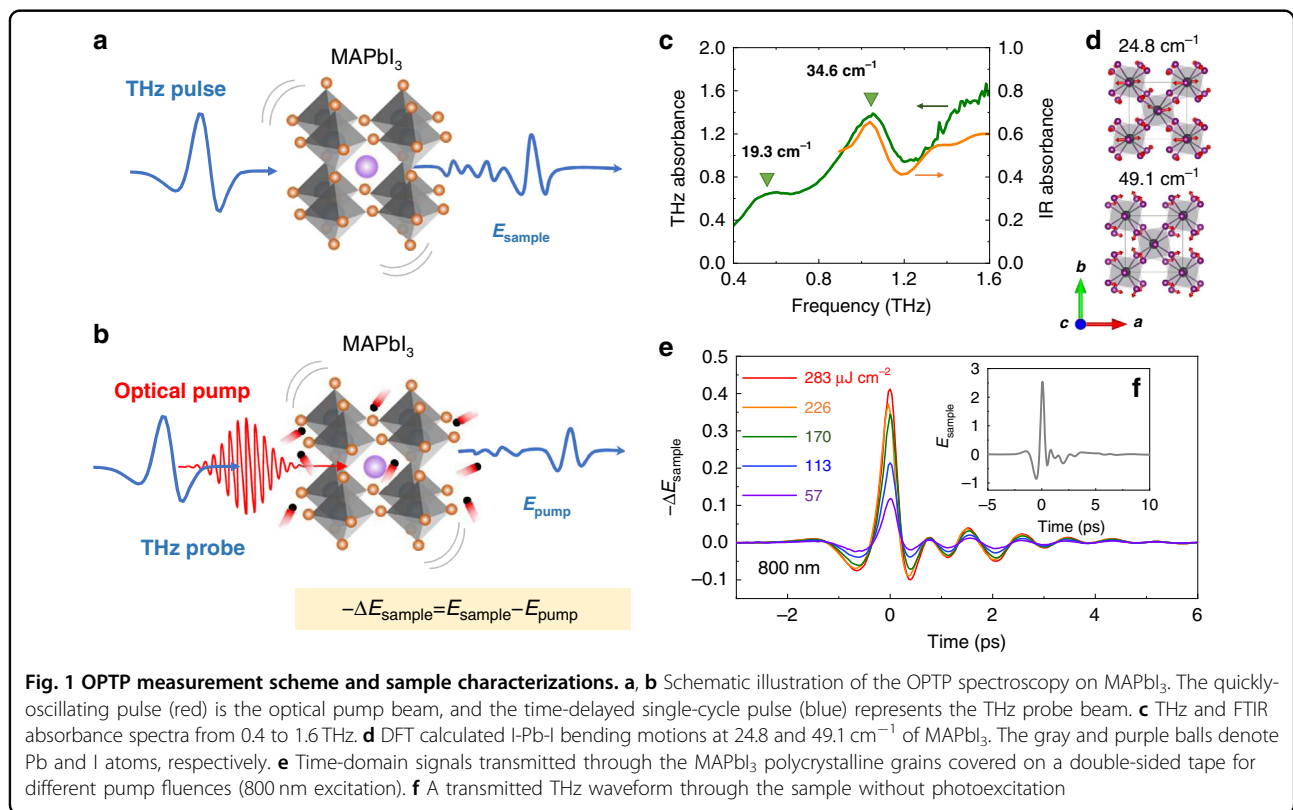
MAPbI₃ single crystal was ground into isotropic polycrystalline grains. The average size of the polycrystalline grains spread on a double-sided adhesive tape is about $10 \pm 5 \mu\text{m}$, which was determined by both optical microscopy and THz near-field optical microscope, as shown in Figs. S3 and S4. As control samples, the details of MAPbI₃ perovskite thin films preparation are shown in Note 3 and Fig. S5 in the Supplemental Materials.

We performed the ultrafast THz conductivity measurement using the OPTP technique, which probes the difference between pre-photoexcited and post-photoexcited THz conductivities of MAPbI₃. As shown in Fig. 1a, b, an 800 nm (photon-energy of 1.55 eV) or a 400 nm (3.1 eV) laser beam was impinging on the MAPbI₃ sample as an optical pump with a spot of $\sim 5 \text{ mm}$ in diameter. The photoexcited conductivity of the sample was probed with a sub-picosecond THz pulse. The transmitted THz probe pulse (containing spectral amplitude and phase information) through the sample was measured by an optical sampling pulse in a $\langle 110 \rangle$ -oriented ZnTe crystal of a thickness of 1 mm (see “Materials and methods”, Fig. S6).

The static THz properties of the unexcited perovskite sample were firstly investigated to elucidate the presence of transverse optical (TO) and longitudinal optical (LO) phonon modes (Fig. 1a), which is associated with the internal vibrations of the PbI₃ framework⁶³. Figure 1c

shows the absorbance properties of the unexcited MAPbI₃ polycrystalline grains, using both Fourier transform infrared spectroscopy (FTIR) and THz time-domain spectroscopy (THz-TDS) (see “Materials and methods” and Fig. S7 for details). Two vibrations in the THz absorbance spectrum around 0.58 THz (19.3 cm^{-1}) and 1.04 THz (34.6 cm^{-1}) originate mainly from the Pb–I inorganic sublattice. The THz absorption peak at 1.04 THz is associated with the IR-active mode. These two low-frequency skeletal bending modes can be assigned to the octahedral twist TO phonon mode and the octahedra distortion LO phonon mode, respectively⁶⁴. We compare the experimental results with the DFT calculations, to elucidate the nature of these lattice vibration modes of MAPbI₃ with tetragonal phase (*I4/mcm*). Figure 1d shows the calculated vibrational displacements for the 24.8 and 49.1 cm^{-1} modes of MAPbI₃, which are composed of I–Pb–I bond bending motions mostly. They are assigned to B_{1g} and A_{1g} mode in the *D*_{4h}¹⁸ symmetry group, respectively. The detailed calculations are shown in Fig. S9. Note that the DFT results show a $\sim 20\%$ deviation below 100 cm^{-1} ⁶⁵. The discrepancy between experimental data and theoretical model results can be attributed to the dynamic disorder of cations, cation rotational unlocking, and local polar fluctuation⁶⁶.

To decipher the coupling of photoexcited carriers with the skeletal bending optical phonons^{67,68}, the sample is



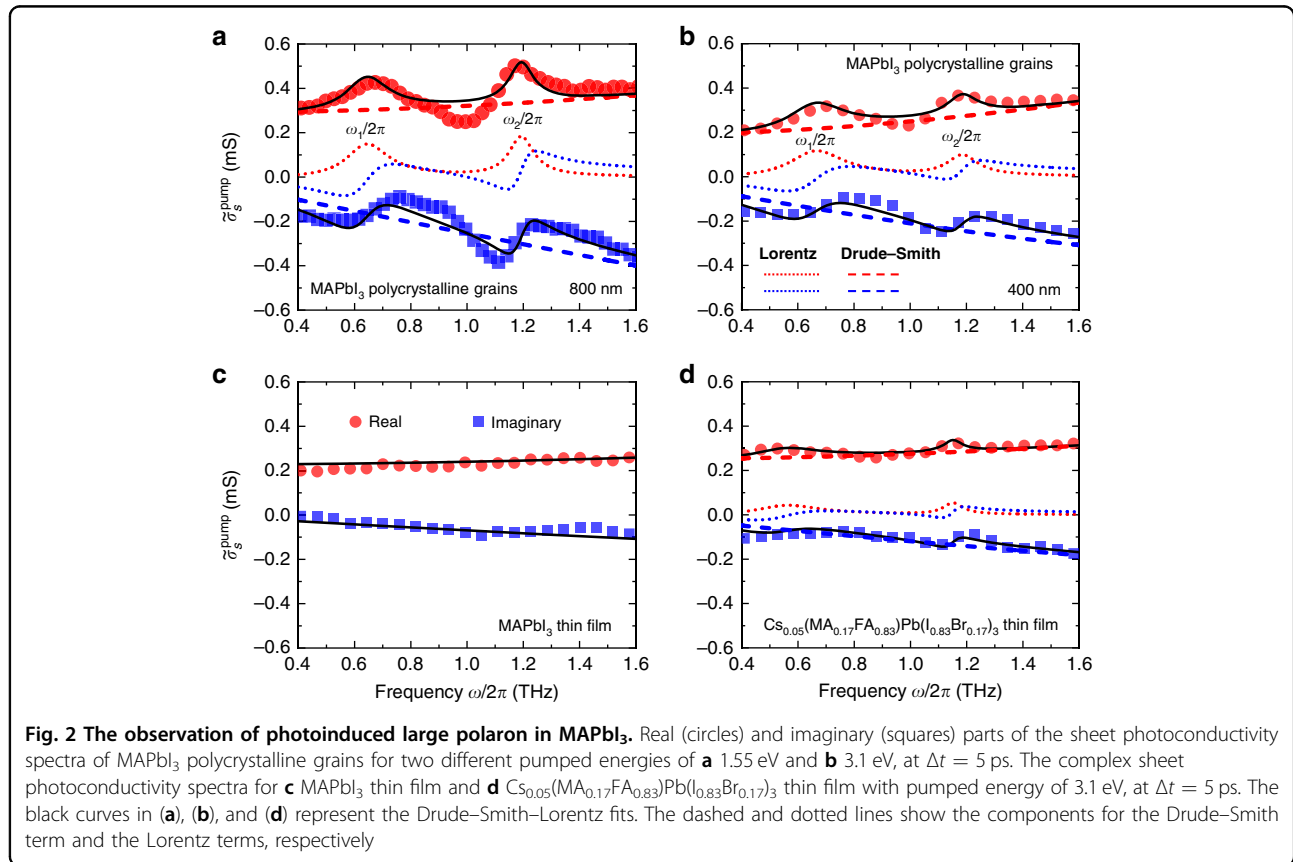
excited by an 800 nm linear polarized pump laser pulse (Fig. 1b). Due to the photoexcitation, the transmitted THz waveform is modified. Figure 1e shows the pump-induced THz electric field change $-\Delta E_{\text{sample}}(t, \Delta t)$, as a function of pump fluence at a given pump-probe time delay of $\Delta t = 5$ ps. Figure 1f shows the time-domain THz waveform transmitted through the sample without photoexcitation, $E_{\text{sample}}(t)$. The frequency-resolved complex sheet photoconductivity $\tilde{\sigma}_s^{\text{pump}}(\omega, \Delta t) = \tilde{\sigma}^{\text{pump}}(\omega, \Delta t) \times d_p$, where $d_p \approx 1 \mu\text{m}$ is the penetration depth⁶⁹. According to the applicability of the thin-film approximation in THz photoconductivity measurements⁷⁰, $\frac{n_2 d_p \omega}{c} \approx 0.01 \ll 1$ for $\omega = 1$ THz and $n_2 = 2.6$ (n_2 is the refractive index of non-photoexcited MAPbI₃ at 300 K⁷¹) indicates that the thin film approximation holds. $\tilde{\sigma}_s^{\text{pump}}(\omega, \Delta t)$ can be extracted by⁷²,

$$\tilde{\sigma}_s^{\text{pump}}(\omega, \Delta t) = \frac{n_1 + n_2}{Z_0} \left(\frac{1}{T^{\text{pump}}(\omega, \Delta t)} - 1 \right) \quad (1)$$

where, $T^{\text{pump}}(\omega, \Delta t) = \frac{E_{\text{pump}}(\omega, \Delta t)}{E_{\text{sample}}(\omega)} = \frac{E_{\text{sample}}(\omega) + \Delta E_{\text{sample}}(\omega, \Delta t)}{E_{\text{sample}}(\omega)}$. $n_1 = 1$ is the refractive index of air. $Z_0 = 377 \Omega$ is the impedance of free space. ω is the THz angular frequencies of the probe electric fields. Note that the distinction

between sheet and volume conductivity does not affect the calculation of the effective large polaron mass and mobility, which will be discussed later.

Figure 2a, b shows the real part $\sigma_{\text{real},s}^{\text{pump}}(\omega)$ and the imaginary part $\sigma_{\text{imag},s}^{\text{pump}}(\omega)$ of the frequency-resolved $\tilde{\sigma}_s^{\text{pump}}(\omega, \Delta t = 5$ ps) of MAPbI₃ polycrystalline grains, acquired at two pump wavelengths of 800 and 400 nm. The pump fluences are $57 \mu\text{J cm}^{-2}$ (800 nm excitation) and $99 \mu\text{J cm}^{-2}$ (400 nm excitation). Generally, the positive $\sigma_{\text{real},s}^{\text{pump}}(\omega)$ grows with the increase in frequency, while the $\sigma_{\text{imag},s}^{\text{pump}}(\omega)$ is negative and decreases with the increasing frequency, in the probed frequency window. The non-Drude spectral response clearly indicates that the free mobile charge is not the only contribution to the signal⁷³. Because the thermal energy of 26 meV at room temperature is higher than the exciton binding energy of MAPbI₃ ($\sim 10\text{--}16$ meV)⁷⁴, excitons are mostly dissociated into free carriers, and therefore any possibility of exciton contribution to the spectrum modulation can be excluded⁷⁵. Since no external fields or electrodes are applied to the material during the measurement, the observed negative $\sigma_{\text{imag},s}^{\text{pump}}(\omega)$ implies the presence of carrier scattering from the crystalline boundaries or defects, as characterized later⁷⁶. It is important to note that, as shown in Fig. 2a,



two resonant peaks in $\sigma_{\text{real},s}^{\text{pump}}(\omega)$ accompanied by two inflection points in $\sigma_{\text{imag},s}^{\text{pump}}(\omega)$ are observed at ~ 0.65 and ~ 1.17 THz, when excited with an 800 nm pump pulse. Similar resonant peaks are observed for the photoexcitation with a 400 nm pump pulse (Fig. 2b). This confirms the robustness of our observations and suggests that the photoconductivity spectrum is similar for band edge- (800 nm) and far-above-gap (400 nm) excitations, despite the difference in the excitation/relaxation channels. For comparison, the photoconductivity spectrum of a solution-processed MAPbI₃ thin film (with grain size of several hundred nanometers) has been measured, as shown in Fig. 2c. No clear THz peaks on $\sigma_{\text{real},s}^{\text{pump}}(\omega)$ are observed, consistent with the spectrum reported in similar MAPbI₃ thin film⁷⁷. This is due to the thermal or structural instabilities for the pure perovskite compound MAPbI₃ thin film. The crystallization quality may be less good in the MAPbI₃ thin film, leading to less strong optical phonon signal. A Drude–Smith (DS) model provides a quantitative description of the localized charge carriers in the MAPbI₃ thin film (see Fig. S10). We further investigate a triple cation mixed halide (Cs)/MA/CH₃(NH₂)₂⁺(FA) thin film with better stability⁷⁸. Figure 2d shows the presence of resonance-like modulations in $\sigma_{\text{real},s}^{\text{pump}}(\omega)$ accompanied by inflection points in $\sigma_{\text{imag},s}^{\text{pump}}(\omega)$ of the Cs_{0.05}(MA_{0.17}FA_{0.83})Pb(I_{0.83}Br_{0.17})₃ thin film (see Fig. S11 for details). The observed feature of resonances in the photoconductivity spectra comes from the coupling the photoexcited charge carriers with the optical phonons of the soft lattice^{79,80}.

To gain more insight into our data, $\tilde{\sigma}_s^{\text{pump}}(\omega)$ is fitted by a DSL model,

$$\tilde{\sigma}_s^{\text{pump}}(\omega) = \frac{\varepsilon_0 \omega_p^2}{\Gamma - i\omega} \left(1 + \frac{c_1}{1 - i\omega/\Gamma} \right) + \sum_m \frac{g_m \omega}{i(\omega_m^2 - \omega^2) + \gamma_m \omega} \quad (2)$$

The first term of Eq. (2) indicates the DS portion, which accounts for the disorder or backscattering induced transport of mobile charge carriers^{81–83}. ε_0 is the vacuum permittivity. The DS term has three free parameters ω_p , c_1 and Γ . ω_p is the Drude plasma frequency. c_1 is the phenomenological localization parameter, which ranges between 0 and -1 . 0 and -1 manifest free-carrier transport and 100% backscattering, respectively. Γ denotes the DS scattering rate of the free carriers, related to the carrier mobility by $\mu = e(1 + c_1)/(\Gamma m_p^*)$, where m_p^* is the effective mass of polarons in MHPs and e is the elementary charge. The second term of Eq. (2) is the Lorentzian portion. g_m , γ_m , and ω_m are the oscillator strength, full-width at half-maximum (FWHM) linewidth, and THz angular frequency of the optical phonon modes m , respectively. Note that the global fitting of DSL model is

performed on both measured $\sigma_{\text{real},s}^{\text{pump}}(\omega)$ and $\sigma_{\text{imag},s}^{\text{pump}}(\omega)$ simultaneously, over the entire measured spectra.

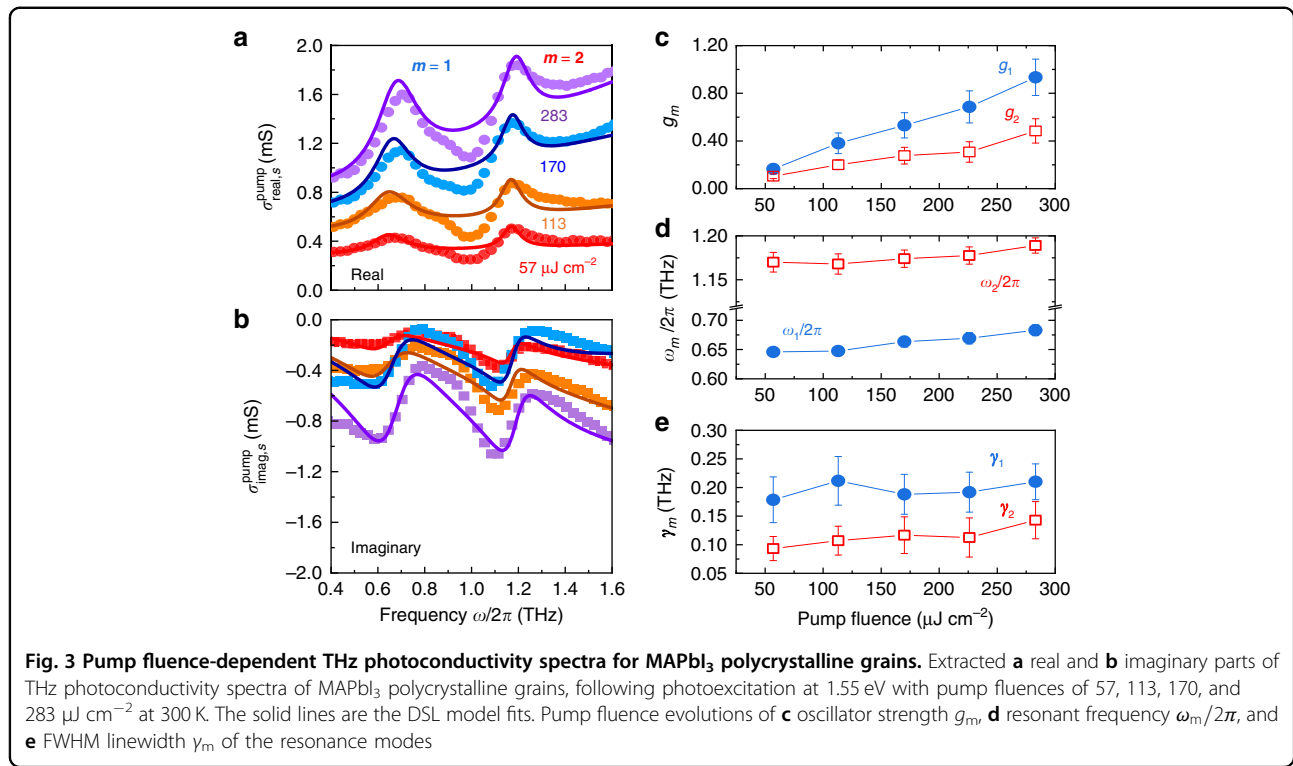
To aid comparison, we separate the DS component (dashed lines) and Lorentz component (dotted lines) of the $\tilde{\sigma}_s^{\text{pump}}(\omega)$ (Fig. 2a, b). The extracted resonance frequencies of the optical phonon modes, $\omega_1/2\pi \approx 21.6$ cm⁻¹, $\omega_2/2\pi \approx 39.0$ cm⁻¹ (800 nm pump), and $\omega_1/2\pi \approx 22.3$ cm⁻¹, $\omega_2/2\pi \approx 39.3$ cm⁻¹ (400 nm pump). Both are blue-shifted compared to the static optical phonon modes of 19.3 and 34.6 cm⁻¹ (Fig. 1c). It is noteworthy that the resonance peaks around 21.6 and 39.0 cm⁻¹ probed by OPTP spectroscopy are in good agreement with the excited-state wave packets oscillating at ~ 21 and ~ 45 cm⁻¹ measured by time-domain Raman spectroscopy³⁹, as well as the strong e-ph coupling at 21.6 and 40 cm⁻¹ obtained by THz emission spectrum⁸⁴.

To further reveal the nature of the e-ph interaction, we analyze the $\tilde{\sigma}_s^{\text{pump}}(\omega)$ using the 800 nm excitation at $\Delta t = 5$ ps with different pump fluences, as shown in Fig. 3a, b. Our experimental results can be well fitted by the DSL model (see Fig. S12 for details of the DS and Lorentz components). Remarkably, the increase of pump fluence modifies the spectral line-shape and amplitude of the resonances. Figure 3c–e summarizes the extracted oscillator strength ($g_{1,2}$), mode frequency ($\omega_{1,2}/2\pi$), and FWHM linewidth ($\gamma_{1,2}$) of two photo-induced optical phonon modes versus the pump fluence. It can be identified that γ_1 is broader than γ_2 , while both are independent of pump fluence within the given uncertainty. $g_{1,2}$ increases upon increasing the pump fluence. In addition, $\omega_1/2\pi$ and $\omega_2/2\pi$ are slightly blue-shifted from 0.65 ± 0.017 to 0.69 ± 0.003 THz and from 1.17 ± 0.019 to 1.19 ± 0.004 THz, respectively, when the pump fluence increases from 57 to 283 $\mu\text{J cm}^{-2}$. According to the DFT simulations, the neutral geometry of perovskite MAPbI₃ is nearly a regular octahedron. Once a charge is introduced into the lattice, it results in a more ionic Pb–I framework and structural distortion, leading to a blueshift of phonon modes⁸⁰. These observations corroborate again our claim that a direct fingerprint of a polaron formation is demonstrated, and will be used below to obtain the effective mass and the mobility of large polaron.

For now, let us concentrate on the effective mass enhancement (compared with the bare band effective mass) of the large polaron in MAPbI₃, due to e–ph interaction at zero magnetic field, first proposed by Feynman^{85–87}

$$m_p^* = m_b^* \left(1 + \frac{\alpha_{\text{e-ph}}}{6} + \frac{\alpha_{\text{e-ph}}^2}{40} + \dots \right) \quad (3)$$

where $m_b^* = 0.1 \times m_0$ (m_0 : the mass of free electron) is the bare band effective mass of electrons in solids, $\alpha_{\text{e-ph}}$ is the dimensionless Fröhlich e–ph coupling constant, given by



the Landau–Pekar model^{43,85,86,88}:

$$\alpha_{e-ph} = \frac{e^2}{4\pi\hbar} \left(\frac{1}{\epsilon_{opt}} - \frac{1}{\epsilon_s} \right) \sqrt{\frac{m_b^*}{2\hbar\omega_{ph}}} \quad (4)$$

here, $\epsilon_{opt} \approx 5.5\epsilon_0$ and $\epsilon_s \approx 30\epsilon_0$ are the optical and static dielectric constants⁶⁷. $\left(\frac{1}{\epsilon_{opt}} - \frac{1}{\epsilon_s}\right)$ qualitatively manifests the capacity of the screening due to a Coulomb potential of the polarized lattice. ω_{ph} is the angular frequency of the LO phonon mode and \hbar is the reduced Planck constant. By using the LO phonon mode of 34.6 cm⁻¹ from our measurement, we obtain $\alpha_{e-ph} \approx 2.64$ in MAPbI₃ polycrystalline grains. This number is significantly larger than 0.07 for GaAs and 0.29 for CdTe, and is smaller than 6, which indicates the formation of large polaron in MAPbI₃ materials⁵⁵. The effective large polaron mass is consequently calculated, $m_p^* = 0.144 m_0$. To proceed, using the mode frequencies of photoinduced LO phonon resonance ($\omega_{ph}/2\pi \approx 39.0 - 39.6$ cm⁻¹) with increased pump fluences, α_{e-ph} decreases by about 6.6% from about 2.64 to 2.46. Meanwhile, m_p^* decreases by about 2% from about 0.144 m_0 to 0.141 m_0 . These numbers fall well within the range of the large polaron mass determined by both magneto-optical spectroscopy^{56,57} and calculations^{89,90}. We would comment that the mass enhancement by polaron effect decreases the mobility by about 30.6%, which cannot exclusively account for the moderate carrier mobility of MAPbI₃. Following the DSL model Eq. (2), the mean

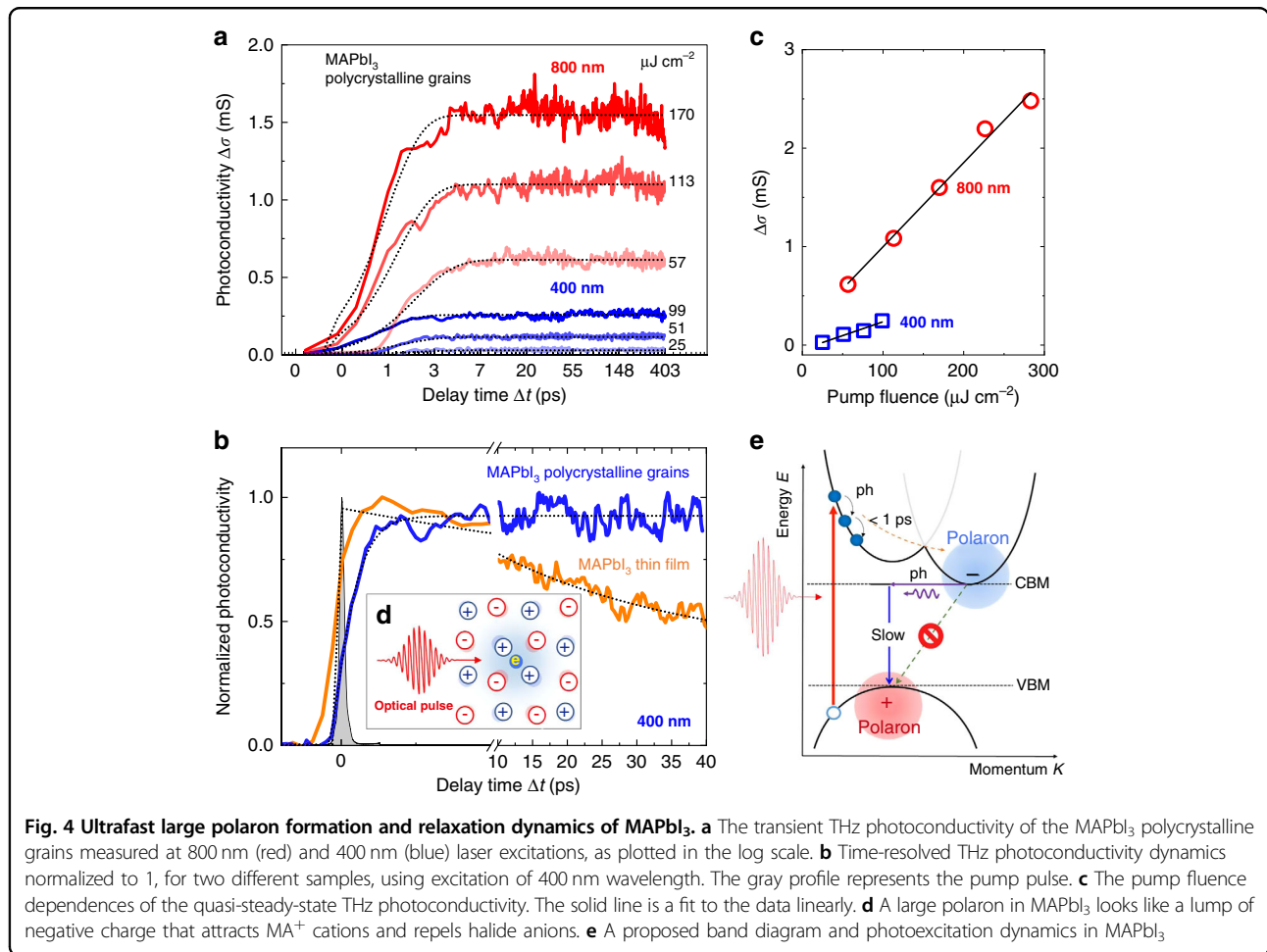
carrier scattering rate $\Gamma \approx 25.8 \pm 6.0$ THz and the localization factor $(1 + c_1) = 0.17 \pm 0.04$ have been extracted (see Fig. S12). The relation $\mu = e(1 + c_1)/(\Gamma m_p^*)$ allows one to calculate the large polaron mobility on the order of $\sim 80.7 \pm 26.0$ cm² V⁻¹ s⁻¹, which reaches up to $\sim 60.7\%$ of the theoretical limit⁵⁵. The localization factor $(1 + c_1)$ due to the back-scattering by grain boundaries or defects further suppresses the mobility by $\sim 83\%$. The mobility value is comparable with the values of MAPbI₃ single crystal and polycrystalline films, measured by both THz and microwave spectroscopy, as summarized in Table 1^{91–96}. We note that the m_p^* used here is not assumed a priori but rather determined experimentally. In our case, both the mass enhancement of large polaron and the boundary or defect scattering account for the relatively low polaron-based mobility in MAPbI₃ polycrystalline grains. It is expected that the polaronic carriers can transport more efficiently with less structural disorder in MAPbI₃.

We now move one step further in our analysis to explore the dynamics of photo-induced large polaron. Figure 4a shows the dynamics of the frequency-averaged photoconductivity $\Delta\sigma(\Delta t)$, measured with different pump fluences of 800 and 400 nm excitations (see “Materials and methods”). As shown in Fig. 4b, compared with the optical pump pulse, the rise of $\Delta\sigma(\Delta t)$ observed in MAPbI₃ polycrystalline grains is slower than the timescale of the instrument-response function (gray). We note that $\Delta\sigma(\Delta t)$ increases in the first 5 ps due to the formation of

Table 1 Comparison of the Fröhlich coupling constant α_{e-ph} , polaron effective mass m_p^* (relative to the band effective mass m_b^*) and mobility measured in MAPbI₃ with that from calculations and measurements in the literatures

Material	α_{e-ph}	m_p^* (%)	Mobility at room temperature (cm ² V ⁻¹ s ⁻¹)	Approach	Theoretical or experimental
MAPbI ₃ polycrystalline grains (this work)	~2.6–2.46	+41–44%	~80.7 ± 26.0	Time-resolved THz spectroscopy	Experimental
MAPbI ₃	2.39	+37%	136	Single-phonon Fröhlich model	Theoretical ⁵⁵
MAPbI ₃	1.4	+28%		Multiphonon Fröhlich polaron model	Theoretical ⁹³
MAPbI ₃	1.91		33	Multi-LO phonon coupling	Theoretical ⁹⁴
MAPbI ₃ thin film	1.72	+35%	197	Far-IR spectroscopy	Experimental ⁸⁵
MAPbI ₃ single crystal	2			Time-resolved multi-THz spectroscopy	Experimental ⁶⁷
MAPbI ₃ thin film			20–75	Time-resolved microwave conductivity	Experimental ⁹⁵
MAPbI ₃ thin film			~25	Time-resolved THz spectroscopy; Time-resolved microwave conductivity	Experimental ⁴⁶
MAPbI ₃ thin film			~27	Time-resolved THz spectroscopy	Experimental ⁵³
MAPbI ₃ single crystals			59	Time-resolved THz spectroscopy	Experimental ⁹⁶
MAPbI ₃ thin film			33		

m_p^* (%): in terms of its increase with respect to the band effective mass



conductive polaronic carriers until a quasi-steady-state is reached, which happens on a different timescale from the generation of free carriers that occurs on sub-100 fs timescales^{97–99}. The slow rise of THz photoconductivity has been attributed to the charge carrier cooling and polaron formation sequentially^{51,73}. A time-dependent polaron population model in ref. 51 is used to fit the rising dynamics of the polycrystalline sample with different pump fluences, as shown the dot lines in Fig. 4a. The time constants for the large polaron formation and the hot electron cooling are ~ 460 and ~ 180 fs, respectively, in good agreement with the values reported for similar MAPbI₃ samples at room temperature⁵¹. Fig. 4c shows the linear dependence of the quasi-steady-state photoconductivity on the pump fluences in the range 25–283 $\mu\text{J cm}^{-2}$, which confirms the investigation of the large polaron in the linear regime. There was no observable photo-degradation and/or thermal damage in the polycrystalline MAPbI₃ sample as the pump fluence reaches up to 1 mJ cm^{-2} . However, there was no direct experimental characterization to clarify it, which will be our future research focus. Importantly, we note that $\tilde{\sigma}_s^{\text{pump}}(\omega)$ measured at $\Delta t = 200$ ps shows a similar spectral characteristic as that measured at 5 ps just after photoexcitation (see Fig. S13). In addition, $\Delta\sigma(\Delta t)$ shows very stable and non-decaying dynamics within 400 ps (limited by current temporal probe window), indicating a very long-lifetime recombination process of large polaron-based carriers in MAPbI₃ polycrystalline grains. In contrast, as the less significant polaronic effect observed in our solution-processed MAPbI₃ thin film, the photoconductivity shows a faster decay and a much shorter lifetime (orange line in Fig. 4b). This behavior is likely caused by the charge trapping due to the defects and imperfections. We conclude that the formation of large polaron in MAPbI₃ polycrystalline grains efficiently protects the charge carriers from being trapped, thus extends the carrier lifetime.

Discussion

First, based on the experimental results, we directly identify the photocarriers-optical phonon coupling in different types of MAPbI₃ samples by OPTP spectroscopy, revealing the underlying large polaron formation. Considering the DSL model and Fröhlich-type large polaron, we demonstrate a straightforward experimental measurement of the effective mass, e–ph coupling constant, which are not presupposed. Using the extracted carrier scattering parameters, we derive the large polaron mobility of MAPbI₃ polycrystalline grains. The moderate polaronic carrier mobility is mainly determined by the enhanced carrier scattering, rather than the polaron mass enhancement. In addition to the partial contribution to the limitation of the intra-grain charge transport, the

presence of large polarons leads to the long charge carrier lifetime in MAPbI₃. Our spectroscopic results of the large polaron formation rationalizes the previously reported contradiction between the long carrier lifetimes (slow electron–hole recombination) and the moderate carrier mobility in MAPbI₃.

Second, our understanding on transport mechanism involving in both polaronic carrier mobility and lifetime in MAPbI₃ provides a unifying picture of photo-excitation and relaxation channels in MAPbI₃ qualitatively. Initially, the photons are absorbed in MAPbI₃ to generate transient excitons, which can be effectively dissociated into free carriers¹⁰⁰. In the real space, owing to the Coulomb interaction, a photo-induced carrier shifts the equilibrium positions of the surrounding anions and cations from their carrier-free positions¹⁰¹. The displacement between ions in the lattice results in a potential well, which traps the photocarriers, as illustrated in Fig. 4d. Within the energy-momentum space (Fig. 4e), the absorbed photons create a Fermi–Dirac distribution, which is thermalized by the carrier–carrier scattering on the 100 fs timescale^{102,103}. The hot-carrier cooling is described as the electrons cascading down to the conduction band minimum, or the holes cascading up to the valence band maximum, exchanging $\sim \text{meV}$ energy with the lattice by LO phonon emission, on the timescale of 100 fs to 1 ps¹⁰⁴. Meanwhile, the large polaron formation occurs at around 460 fs. The enhanced screening weakens the large polaron scattering with other carriers, defects, and LO phonons. Because of the inhibited LO-phonon emission, hot electron energy is retained and hot polarons are formed. The slow recombination of hot polarons that occurs on hundreds of picoseconds can be explained by the low thermal conductivity of MAPbI₃^{105,106}. As the length of charge diffusion is determined by the carrier recombination lifetime, the charge extraction is still suitable, despite the polaron mobility is relatively low. Thus, insights into the large polarons in the nonequilibrium higher energy states are crucial for developing efficient hot carrier-based optoelectronic applications¹⁰⁷. As such, with the advance in device fabrication and characterization of MHPs using femtosecond laser techniques, the photo-degradation and transient laser heating effect need to be addressed and will be the topic of future work.

Finally, we would comment that the experimental results are discussed in the framework of the Fröhlich polaron, which is based on the harmonic approximation. While, due to the dynamic disordered properties of the MAPbI₃ lattice, the local electric field can produce local ordering of polar nanodomains surrounding the photocarriers¹⁰⁸. Therefore, from the theoretical perspective, a more accurate model with local ferroelectric-like large polarons (including anharmonic and dynamical disorder effects)¹⁰⁹ is desired to microscopically visualize the

dynamics of large polarons. Furthermore, experimental efforts of optical pump-THz near field microscopy are required to characterize the transport of large polarons affected by defects and grain boundaries^{110–112}.

In summary, the THz photoconductivity spectra of MAPbI₃ polycrystalline grains have been modeled by the DS model augmented by Lorentzian terms, accounting for the fingerprint of optical phonon modes coupled to the photogenerated carriers. From our analysis that combines DSL model and Fröhlich-type large polaron, no prior knowledges about the effective mass and scattering events are required to experimentally derive the large polaron mobility of MAPbI₃. In addition, the formation of large polarons results in much longer charge carrier lifetime in polycrystalline MAPbI₃, which is attributed to the efficient protection of band-edge carriers by self-trapping potential and low thermal conductivity. Our work adds to the fundamental understanding on the polaronic nature of charge carriers in MAPbI₃ at room temperature, which is essential to their optoelectronic properties and applications.

Materials and methods

Samples preparation

To synthesize CH₃NH₃I (MAI), 24 mL of methylamine (33 wt% dissolved in EtOH), 10 mL of hydroiodic acid (57 wt% dissolved in H₂O), and 100 mL of EtOH were added into a 250 mL-round bottom flask. The reaction took place under Ar gas at 0 °C for 2 h upon stirring. After reaction, a white product MAI was collected by rotary evaporation in a water-bath of 50 °C. Thereafter, the MAI precipitate was dissolved in EtOH and then underwent sedimentation in diethyl ether upon stirring for 30 min. After that, single crystals of MAPbI₃ were prepared by first mixing PbI₂ and MAI solution homogeneously at a high temperature and then slowly cooling it down to an ambient temperature. Since the THz pulse can hardly transmit through a thick crystal, the MAPbI₃ single crystal was ground into polycrystalline grains for the following investigation.

Terahertz (THz) time-domain spectroscopy (THz-TDS)

Broadband THz-TDS was carried out on the MAPbI₃ polycrystalline grains with the EKSPLA system. Femto-second laser pulse (150 mW, 100 fs duration, 800 nm wavelength, 76 MHz repetition rate) was split into two beams: generation and detection laser beam. The generation beam was focused on a low temperature grown (LTG) GaAs photoconductive emitter. The generation beam was modulated by an optical chopper. The generated THz beam is focused by paraboloidal mirrors and transmitted through the MAPbI₃ polycrystalline grains. The detection laser beam through a delay stage was used to record the THz waveform by another LTG GaAs

photoconductive detector. The signal to noise ratio is better than 1000:1. All the static THz spectra were performed in the drying air environment at room temperature. The refractive index and absorption coefficient of the double-sided adhesive tape are shown in Fig. S8.

Optical pump/THz electromagnetic probe (OPTP) spectroscopy

The OPTP system is driven by a Ti:sapphire fs amplifier laser pulse of ~120 fs duration with a repetition rate of 1 kHz. The laser beam was split into three arms: a pump beam, a THz probe beam, and an electro-optic sampling (EOS) beam (see Fig. S6). An 800 nm or 400 nm pump beam was used to photoexcite the MAPbI₃ sample within a ~5 mm diameter area, ensuring a homogeneous pumping condition. The 400 nm pump beam is produced by second harmonic generation based on the 800 nm beam by beta barium borate (BBO) crystal. The time-resolved photo-induced complex THz conductivity spectra were interrogated using a time-delayed freely propagating THz probe transient with a ~1 ps-long optical cycle. The THz probe pulse was generated by an optical rectification crystal ZnTe (<110> orientation, 10 mm × 10 mm × 1 mm thickness), which was pumped with a slightly focused 800 nm laser beam. The THz beam was focused on the sample (~3 mm in diameter) using a pair of off-axis parabolic mirrors. The THz electric field accelerates the photocarriers, leading to an attenuation of the THz electric field. The transmitted THz pulses through the sample were recollimated and focused onto a second 1 mm-thick <110> ZnTe by another pair of parabolic mirrors. The modulated THz electric fields were coherently recorded by the free-space EOS beam, using a Wollaston prism, a pair of balanced photodiodes and a lock-in amplifier. Our OPTP setup is free of any spot-size effect and it is a homogeneous excitation for all frequencies in the THz pulse bandwidth. A custom-made drying air-flow chamber was used to prevent humidity-degradation of the MAPbI₃ samples during the measurement as much as possible. No obvious observation of photodegradation and/or thermal damage was found during a 12 h experiment period. However, there was no further experimental characterization to clarify it. We also note that no photo-induced change can be observed in the THz transmission for a single double-sided tape. All measurements were performed at room temperature.

Theoretical calculations of vibrational frequencies

We carried out the structural optimization and phonon calculations of MAPbI₃ using the first principles within the framework of density functional theory (DFT). We used the DFT software of Vienna ab initio simulation package based on the projector augmented wave method. We treated the exchange-correlation interaction in the

DFT calculations using the generalized gradient approximation which is proposed by Perdew, Burke, and Ernzerhof (PBE). We adopted a $\sqrt{2} \times \sqrt{2} \times 2$ MAPbI₃ unit cell for structural optimization and phonon calculations. During the DFT simulations, we used the energy cutoff of 500 eV and a Monkhorst–Pack grid with $4 \times 4 \times 4$ k-points. We set the convergence criterion of Hellman–Feynman force as $0.01 \text{ eV } \text{Å}^{-1}$ during the structural optimization. We used the density functional perturbation theory (DFPT) method to calculate the phonon frequencies and eigenvectors for Γ point of MAPbI₃. The phonon vibrational displacements of the vibrational modes 24.8, 49.1, and 82.9 cm^{-1} are listed in Fig. S9 and Table S2.

Acknowledgements

This work at University of Shanghai for Science and Technology is supported by the National Natural Science Foundation of China (NSFC, Grants No. 61988102, No. 61975110, No. 61735010); the 111 Project (Grant No. D18014); The Key project supported by Science and Technology Commission Shanghai Municipality (Grant No. YDZX20193100004960). Science and Technology Commission of Shanghai Municipality (Shanghai Rising-Star Program Grant No. 18QA1401700). General Administration of Customs People's Republic of China (Grant No. 2019HK006). Shanghai Educational Development Foundation (Grant No. 16CG45).

Author details

¹Terahertz Technology Innovation Research Institute, Terahertz Spectrum and Imaging Technology Cooperative Innovation Center, Shanghai Key Lab of Modern Optical System, University of Shanghai for Science and Technology, Shanghai 200093, China. ²Qingdao Institute of Bioenergy and Bioprocess Technology, Chinese Academy of Sciences, Qingdao 266101, China. ³Physics Department, Materials Genome Institute, State Key Laboratory of Advanced Special Steel, Shanghai Key Laboratory of High Temperature Superconductors, International Centre of Quantum and Molecular Structures, Shanghai University, Shanghai 200444, China. ⁴Shanghai Institute of Technical Physics, Chinese Academy of Sciences, Yutian Road 500, Shanghai, China. ⁵Department of Physics, Shanghai University, 99 Shangda Road, Shanghai 200444, China. ⁶University of Michigan – Shanghai Jiao Tong University Joint Institute, Shanghai Jiao Tong University, Shanghai, China. ⁷School of Physics, University of Wollongong, Wollongong, NSW 2522, Australia. ⁸Department of Physics and International Laser Center, Lomonosov Moscow State University, Leninskie Gory 1, Moscow 19991, Russia. ⁹LIT RAS-Branch of the FSRC «Crystallography and Photonics» RAS, Svyatoozerskaya 1, 140700, Shatura, Moscow Region, Russia

Author contributions

Z.J. and Y.Z. conceived the idea and designed the experiments. Z.L. synthesized the MAPbI₃ materials under the supervision of X.B. Y.F. and Z.Y. performed the terahertz measurements under the supervision of Z.J. and Y.P., H.G., and W.R. performed the DFT calculations. Z.J., Y.P., Z.F., J.W., G.M., Q.C., C.Z., A.B., A.S., Y.Z., and S.Z. analyzed the results and provided the plots. All authors commented on the manuscript.

Data availability

The data that support the findings of this study are available from the corresponding author upon reasonable request.

Conflict of interest

The authors declare no competing interests.

Supplementary information The online version contains supplementary material available at <https://doi.org/10.1038/s41377-022-00872-y>.

Received: 19 January 2022 Revised: 31 May 2022 Accepted: 2 June 2022
Published online: 06 July 2022

References

- Green, M. A., Ho-Baillie, A. & Snaith, H. J. The emergence of perovskite solar cells. *Nat. Photonics* **8**, 506–514 (2014).
- Nie, W. Y. et al. High-efficiency solution-processed perovskite solar cells with millimeter-scale grains. *Science* **347**, 522–525 (2015).
- Biewald, A. et al. Temperature-dependent ambipolar charge carrier mobility in large-crystal hybrid halide perovskite thin films. *ACS Appl. Mater. Interfaces* **11**, 20838–20844 (2019).
- Stranks, S. D. & Snaith, H. J. Metal-halide perovskites for photovoltaic and light-emitting devices. *Nat. Nanotechnol.* **10**, 391–402 (2015).
- Hutter, E. M. et al. Direct–indirect character of the bandgap in methylammonium lead iodide perovskite. *Nat. Mater.* **16**, 115–120 (2017).
- Manser, J. S., Christians, J. A. & Kamat, P. V. Intriguing optoelectronic properties of metal halide perovskites. *Chem. Rev.* **116**, 12956–13008 (2016).
- Xing, G. C. et al. Long-range balanced electron- and hole-transport lengths in organic-inorganic CH₃NH₃PbI₃. *Science* **342**, 344–347 (2013).
- Stranks, S. D. et al. Electron–hole diffusion lengths exceeding 1 micrometer in an organometal trihalide perovskite absorber. *Science* **342**, 341–344 (2013).
- Dong, Q. F. et al. Electron–hole diffusion lengths > 175 μm in solution-grown CH₃NH₃PbI₃ single crystals. *Science* **347**, 967–970 (2015).
- Kang, J. & Wang, W. L. High defect tolerance in lead halide perovskite CsPbBr₃. *J. Phys. Chem. Lett.* **8**, 489–493 (2017).
- You, J. B. et al. Improved air stability of perovskite solar cells via solution-processed metal oxide transport layers. *Nat. Nanotechnol.* **11**, 75–81 (2016).
- Dou, L. T. et al. Solution-processed hybrid perovskite photodetectors with high detectivity. *Nat. Commun.* **5**, 5404 (2014).
- Brenner, T. M. et al. Hybrid organic–inorganic perovskites: Low-cost semiconductors with intriguing charge-transport properties. *Nat. Rev. Mater.* **1**, 15007 (2016).
- Zhang, W., Eperon, G. E. & Snaith, H. J. Metal halide perovskites for energy applications. *Nat. Energy* **1**, 16048 (2016).
- Fang, H. H. et al. Photoexcitation dynamics in solution-processed formamidinium lead iodide perovskite thin films for solar cell applications. *Light: Sci. Appl.* **5**, e16056 (2016).
- Kang, S. B. et al. Stretchable and colorless freestanding microwire arrays for transparent solar cells with flexibility. *Light: Sci. Appl.* **8**, 121 (2019).
- Akerman, Q. A. et al. Strongly emissive perovskite nanocrystal inks for high-voltage solar cells. *Nat. Energy* **2**, 16194 (2017).
- Rogach, A. L. Towards next generation white LEDs: Optics-electronics synergistic effect in a single-layer heterophase halide perovskite. *Light: Sci. Appl.* **10**, 46 (2021).
- Zhang, L. et al. High-performance quasi-2D perovskite light-emitting diodes: from materials to devices. *Light: Sci. Appl.* **10**, 61 (2021).
- Giovanni, D. et al. Origins of the long-range exciton diffusion in perovskite nanocrystal films: Photon recycling vs exciton hopping. *Light: Sci. Appl.* **10**, 2 (2021).
- Xie, C. et al. Ultrasensitive broadband phototransistors based on perovskite/organic-semiconductor vertical heterojunctions. *Light: Sci. Appl.* **6**, e17023 (2017).
- Xing, J. et al. Modulating the optical and electrical properties of MAPbBr₃ single crystals via voltage regulation engineering and application in memristors. *Light: Sci. Appl.* **9**, 111 (2020).
- Giovanni, D. et al. Ultrafast long-range spin-funneling in solution-processed Ruddlesden–Popper halide perovskites. *Nat. Commun.* **10**, 3456 (2019).
- Chen, Z., Dong, G. P. & Qiu, J. R. Ultrafast pump-probe spectroscopy—A powerful tool for tracking spin-quantum dynamics in metal halide perovskites. *Adv. Quantum Technol.* **4**, 2100052 (2021).
- Huang, J. S. et al. Understanding the physical properties of hybrid perovskites for photovoltaic applications. *Nat. Rev. Mater.* **2**, 17042 (2017).
- Saba, M. et al. Excited state properties of hybrid perovskites. *Acc. Chem. Res.* **49**, 166–173 (2016).
- Wright, A. D. et al. Electron-phonon coupling in hybrid lead halide perovskites. *Nat. Commun.* **7**, 11755 (2016).
- Maiti, A. & Pal, A. J. Carrier recombination in CH₃NH₃PbI₃: Why is it a slow process?. *Rep. Prog. Phys.* **85**, 024501 (2022).

29. Zhu, X. Y. & Podzorov, V. Charge carriers in hybrid organic–inorganic lead halide perovskites might be protected as large polarons. *J. Phys. Chem. Lett.* **6**, 4758–4761 (2015).
30. Chen, Y. et al. Extended carrier lifetimes and diffusion in hybrid perovskites revealed by Hall effect and photoconductivity measurements. *Nat. Commun.* **7**, 12253 (2016).
31. Miyata, K., Atallah, T. L. & Zhu, X. Y. Lead halide perovskites: Crystal-liquid duality, phonon glass electron crystals, and large polaron formation. *Sci. Adv.* **3**, e1701469 (2017).
32. Miyata, K. et al. Large polarons in lead halide perovskites. *Sci. Adv.* **3**, e1701217 (2017).
33. Puppini, M. et al. Evidence of large polarons in photoemission band mapping of the perovskite semiconductor CsPbBr₃. *Phys. Rev. Lett.* **124**, 206402 (2020).
34. Evans, T. J. S. et al. Competition between hot-electron cooling and large polaron screening in CsPbBr₃ perovskite single crystals. *J. Phys. Chem. C* **122**, 13724–13730 (2018).
35. Zhu, H. M. et al. Screening in crystalline liquids protects energetic carriers in hybrid perovskites. *Science* **353**, 1409–1413 (2016).
36. Guzelurk, B. et al. Visualization of dynamic polaronic strain fields in hybrid lead halide perovskites. *Nat. Mater.* **20**, 618–623 (2021).
37. Yang, Y. et al. Low surface recombination velocity in solution-grown CH₃NH₃PbBr₃ perovskite single crystal. *Nat. Commun.* **6**, 7961 (2015).
38. Wang, H. et al. Coulomb screening and coherent phonon in methylammonium lead iodide perovskites. *J. Phys. Chem. Lett.* **7**, 3284–3289 (2016).
39. Park, M. et al. Excited-state vibrational dynamics toward the polaron in methylammonium lead iodide perovskite. *Nat. Commun.* **9**, 2525 (2018).
40. Duan, H. G. et al. Photoinduced vibrations drive ultrafast structural distortion in lead halide perovskite. *J. Am. Chem. Soc.* **142**, 16569–16578 (2020).
41. Chen, T. R. et al. Origin of long lifetime of band-edge charge carriers in organic–inorganic lead iodide perovskites. *Proc. Natl Acad. Sci. USA* **114**, 7519–7524 (2017).
42. Meggiolaro, D. et al. Polarons in metal halide perovskites. *Adv. Energy Mater.* **10**, 1902748 (2020).
43. Franchini, C. et al. Polarons in materials. *Nat. Rev. Mater.* **6**, 560–586 (2021).
44. Shrivastava, M. et al. Polaron and spin dynamics in organic–inorganic lead halide perovskite nanocrystals. *Adv. Opt. Mater.* **8**, 2001016 (2020).
45. Zheng, F. & Wang, L. W. Large polaron formation and its effect on electron transport in hybrid perovskites. *Energy Environ. Sci.* **12**, 1219–1230 (2019).
46. Ponceca, C. S. Jr et al. Organometal halide perovskite solar cell materials rationalized: ultrafast charge generation, high and microsecond-long balanced mobilities, and slow recombination. *J. Am. Chem. Soc.* **136**, 5189–5192 (2014).
47. Yettapu, G. R. et al. Terahertz conductivity within colloidal CsPbBr₃ perovskite nanocrystals: Remarkably high carrier mobilities and large diffusion lengths. *Nano Lett.* **16**, 4838–4848 (2016).
48. Miyata, K. & Zhu, X. Y. Ferroelectric large polarons. *Nat. Mater.* **17**, 379–381 (2018).
49. La-o-Vorakiat, C. et al. Phonon mode transformation across the orthorhombic–tetragonal phase transition in a lead iodide perovskite CH₃NH₃PbI₃: A terahertz time-domain spectroscopy approach. *J. Phys. Chem. Lett.* **7**, 1–6 (2016).
50. Maeng, I. et al. Unusual terahertz-wave absorptions in δ/a -mixed-phase FAPbI₃ single crystals: Interfacial phonon vibration modes. *NPG Asia Mater.* **13**, 75 (2021).
51. Bretschneider, S. A. et al. Quantifying polaron formation and charge carrier cooling in lead-iodide perovskites. *Adv. Mater.* **30**, 1707312 (2018).
52. Bonn, M. et al. Role of dielectric drag in polaron mobility in lead halide perovskites. *ACS Energy Lett.* **2**, 2555–2562 (2017).
53. Karakus, M. et al. Phonon–electron scattering limits free charge mobility in methylammonium lead iodide perovskites. *J. Phys. Chem. Lett.* **6**, 4991–4996 (2015).
54. Thongnum, A. & Pinsook, U. Polaron transport in hybrid CH₃NH₃PbI₃ perovskite thin films. *Nanoscale* **12**, 14112–14119 (2020).
55. Frost, J. M. Calculating polaron mobility in halide perovskites. *Phys. Rev. B* **96**, 195202 (2017).
56. Miyata, A. et al. Direct measurement of the exciton binding energy and effective masses for charge carriers in organic–inorganic tri-halide perovskites. *Nat. Phys.* **11**, 582–587 (2015).
57. Yamada, Y. et al. Polaron masses in CH₃NH₃Pb X₃ perovskites determined by Landau level spectroscopy in low magnetic fields. *Phys. Rev. Lett.* **126**, 237401 (2021).
58. Ulbricht, R. et al. Carrier dynamics in semiconductors studied with time-resolved terahertz spectroscopy. *Rev. Mod. Phys.* **83**, 029901 (2011).
59. Zhao, D. M. & Chia, E. E. M. Free carrier, exciton, and phonon dynamics in lead-halide perovskites studied with ultrafast terahertz spectroscopy. *Adv. Optical Mater.* **8**, 1900783 (2020).
60. Wang, X. et al. Ultrafast ionizing radiation detection by p–n junctions made with single crystals of solution-processed perovskite. *Adv. Electron. Mater.* **4**, 1800237 (2018).
61. Xu, Y. et al. Solution-processed epitaxial growth of MAPbI₃ single-crystal films for highly stable photodetectors. *Front. Mater.* **8**, 651957 (2021).
62. Bao, X. C. et al. Efficient planar perovskite solar cells with large fill factor and excellent stability. *J. Power Sources* **297**, 53–58 (2015).
63. Zhao, D. M. et al. Monitoring electron–phonon interactions in lead halide perovskites using time-resolved THz spectroscopy. *ACS Nano* **13**, 8826–8835 (2019).
64. Pérez-Osorio, M. A. et al. Vibrational properties of the organic–inorganic halide perovskite CH₃NH₃PbI₃ from theory and experiment: Factor group analysis, first-principles calculations, and low-temperature infrared spectra. *J. Phys. Chem. C* **119**, 25703–25718 (2015).
65. Leguy, A. M. A. et al. Dynamic disorder, phonon lifetimes, and the assignment of modes to the vibrational spectra of methylammonium lead halide perovskites. *Phys. Chem. Chem. Phys.* **18**, 27051–27066 (2016).
66. Park, M. et al. Critical role of methylammonium librational motion in methylammonium lead iodide (CH₃NH₃PbI₃) perovskite photochemistry. *Nano Lett.* **17**, 4151–4157 (2017).
67. Lan, Y. et al. Ultrafast correlated charge and lattice motion in a hybrid metal halide perovskite. *Sci. Adv.* **5**, eaaw5558 (2019).
68. La-o-Vorakiat, C. et al. Elucidating the role of disorder and free-carrier recombination kinetics in CH₃NH₃PbI₃ perovskite films. *Nat. Commun.* **6**, 7903 (2015).
69. Valverde-Chávez, D. A. et al. Intrinsic femtosecond charge generation dynamics in single crystal CH₃NH₃PbI₃. *Energy Environ. Sci.* **8**, 3700–3707 (2015).
70. Neu, J. et al. Applicability of the thin-film approximation in terahertz photoconductivity measurements. *Appl. Phys. Lett.* **113**, 233901 (2018).
71. Löper, P. et al. Complex refractive index spectra of CH₃NH₃PbI₃ perovskite thin films determined by spectroscopic ellipsometry and spectrophotometry. *J. Phys. Chem. Lett.* **6**, 66–71 (2015).
72. Jin, Z. M. et al. Ultrafast terahertz photoconductivity of photovoltaic polymer–fullerene blends: A comparative study correlated with photovoltaic device performance. *J. Phys. Chem. Lett.* **5**, 3662–3668 (2014).
73. Wang, M. C. et al. Photo-induced enhancement of lattice fluctuations in metal-halide perovskites. *Nat. Commun.* **13**, 1019 (2022).
74. Tilchin, J. et al. Hydrogen-like Wannier–Mott excitons in single crystal of methylammonium lead bromide perovskite. *ACS Nano* **10**, 6363–6371 (2016).
75. Luo, L. et al. Ultrafast terahertz snapshots of excitonic Rydberg states and electronic coherence in an organometal halide perovskite. *Nat. Commun.* **8**, 15565 (2017).
76. Smith, N. V. Classical generalization of the Drude formula for the optical conductivity. *Phys. Rev. B* **64**, 155106 (2001).
77. Xia, C. Q. et al. Ultrafast photo-induced phonon hardening due to Pauli blocking in MAPbI₃ single-crystal and polycrystalline perovskites. *J. Phys.: Mater.* **4**, 044017 (2021).
78. Saliba, M. et al. Cesium-containing triple cation perovskite solar cells: improved stability, reproducibility and high efficiency. *Energy Environ. Sci.* **9**, 1989–1997 (2016).
79. Folpini, G. et al. Ultrafast charge carrier dynamics in quantum confined 2D perovskite. *J. Chem. Phys.* **152**, 214705 (2020).
80. Cinquanta, E. et al. Ultrafast THz probe of photoinduced polarons in lead-halide perovskites. *Phys. Rev. Lett.* **122**, 166601 (2019).
81. Cocker, T. L. et al. Microscopic origin of the Drude–Smith model. *Phys. Rev. B* **96**, 205439 (2017).
82. Kuzel, P. & Němec, H. Terahertz spectroscopy of nanomaterials: A close look at charge-carrier transport. *Adv. Optical Mater.* **8**, 1900623 (2020).
83. Zhang, H. et al. Highly mobile hot holes in Cs₂AgBiBr₆ double perovskite. *Sci. Adv.* **7**, eabj9066 (2021).
84. Guzelurk, B. et al. Terahertz emission from hybrid perovskites driven by ultrafast charge separation and strong electron–phonon coupling. *Adv. Mater.* **30**, 1704737 (2018).

85. Sendner, M. et al. Optical phonons in methylammonium lead halide perovskites and implications for charge transport. *Mater. Horiz.* **3**, 613–620 (2016).
86. Zhang, H. et al. Highly mobile large polarons in black phase CsPbI₃. *ACS Energy Lett.* **6**, 568–573 (2021).
87. Feynman, R. P. Slow electrons in a polar crystal. *Phys. Rev.* **97**, 660–665 (1955).
88. Zheng, W. H. et al. Band transport by large Fröhlich polarons in Mxenes. *Nat. Phys.* **18**, 544–550 (2022).
89. Menéndez-Proupin, E. et al. Self-consistent relativistic band structure of the CH₃NH₃PbI₃ perovskite. *Phys. Rev. B* **90**, 045207 (2014).
90. Fang, H. H. et al. Photophysics of organic–inorganic hybrid lead iodide perovskite single crystals. *Adv. Funct. Mater.* **25**, 2378–2385 (2015).
91. Milot, R. L. et al. Temperature-dependent charge-carrier dynamics in CH₃NH₃PbI₃ perovskite thin films. *Adv. Funct. Mater.* **25**, 6218–6227 (2015).
92. Buizza, L. R. V. & Herz, L. M. Polarons and charge localization in metal-halide semiconductors for photovoltaic and light-emitting devices. *Adv. Mater.* **33**, 2007057 (2021).
93. Schlipf, M., Poncé, S. & Giustino, F. Carrier lifetimes and polaronic mass enhancement in the hybrid halide perovskite CH₃NH₃PbI₃ from multi-phonon Fröhlich coupling. *Phys. Rev. Lett.* **121**, 086402 (2018).
94. Poncé, S., Schlipf, M. & Giustino, F. Origin of low carrier mobilities in halide perovskites. *ACS Energy Lett.* **4**, 456–463 (2019).
95. Oga, H. et al. Improved understanding of the electronic and energetic landscapes of perovskite solar cells: High local charge carrier mobility, reduced recombination, and extremely shallow traps. *J. Am. Chem. Soc.* **136**, 13818–13825 (2014).
96. Xia, C. Q. et al. Limits to electrical mobility in lead-halide perovskite semiconductors. *J. Phys. Chem. Lett.* **12**, 3607–3617 (2021).
97. Manser, J. S. & Kamat, P. V. Band filling with free charge carriers in organo-metal halide perovskites. *Nat. Photonics* **8**, 737–743 (2014).
98. Piatkowski, P. et al. Unraveling charge carriers generation, diffusion, and recombination in formamidinium lead triiodide perovskite polycrystalline thin film. *J. Phys. Chem. Lett.* **7**, 204–210 (2016).
99. Shi, J. J. et al. From ultrafast to ultraslow: charge-carrier dynamics of perovskite solar cells. *Joule* **2**, 879–901 (2018).
100. Ghosh, T. et al. Free carrier emergence and onset of electron-phonon coupling in methylammonium lead halide perovskite films. *J. Am. Chem. Soc.* **139**, 18262–18270 (2017).
101. Emin, D. *Polarons* (Cambridge University Press, 2012).
102. Wong, W. P. D. et al. Large polaron self-trapped states in three-dimensional metal-halide perovskites. *ACS Mater. Lett.* **2**, 20–27 (2020).
103. Tantardini, C. et al. “Self-trapping” in solar cell hybrid inorganic–organic perovskite absorbers. *Appl. Mater. Today* **26**, 101380 (2022).
104. Fu, J. H. et al. Hot carrier cooling mechanisms in halide perovskites. *Nat. Commun.* **8**, 1300 (2017).
105. Joshi, P. P., Maehlein, S. F. & Zhu, X. Y. Dynamic screening and slow cooling of hot carriers in lead halide perovskites. *Adv. Mater.* **31**, 1803054 (2019).
106. Frost, J. M., Whalley, L. D. & Walsh, A. Slow cooling of hot polarons in halide perovskite solar cells. *ACS Energy Lett.* **2**, 2647–2652 (2017).
107. Ahmed, I. et al. There is plenty of room at the top: Generation of hot charge carriers and their applications in perovskite and other semiconductor-based optoelectronic devices. *Light: Sci. Appl.* **10**, 174 (2021).
108. Wang, F. F. et al. Solvated electrons in solids-ferroelectric large polarons in lead halide perovskites. *J. Am. Chem. Soc.* **143**, 5–16 (2021).
109. Schilcher, M. J. et al. The significance of polarons and dynamic disorder in halide perovskites. *ACS Energy Lett.* **6**, 2162–2173 (2021).
110. Semonin, O. E. et al. Limits of carrier diffusion in *n*-type and *p*-type CH₃NH₃PbI₃ perovskite single crystals. *J. Phys. Chem. Lett.* **7**, 3510–3518 (2016).
111. van Hoof, N. J. J. et al. Time-resolved terahertz time-domain near-field microscopy. *Opt. Express* **26**, 32118–32129 (2018).
112. Guo, Z. et al. Long-range hot-carrier transport in hybrid perovskites visualized by ultrafast microscopy. *Science* **356**, 59–62 (2017).